





Progressive underplating of mafic material at mid-crustal depth beneath Ischia volcano, Italy

Irene Bianchi ¹, Giuseppe Pezzo ², Guido Giordano³ & Claudio Chiarabba ²

The destructive (Mw 3.9) earthquake of 21 August 2017 re-opened the question on where magma resides at the Ischia island volcano. The peculiar complexity of the seismic source initiated the debate on the involvement of fluid-related processes, but the magmatic origin of the event remains uncertain. Here we use ground displacement and broadband seismic data to investigate the magmatic system of Ischia volcano, where progressive underplating of mafic material at mid-crustal depth feeds the deep structures, which are characterized by exceptionally high seismic velocity and are connected with a shallow crystal mush. Although no direct evidence of large molten volumes was found, strong anisotropy suggests that the crystal mush is pervaded by magma-intruded dykes. We propose that the 2017 event was due to a negative tensile deformation caused by depressurization of supercritical fluids along a shallow southwest (SW-)dipping fault defined by receiver functions (RFs) data, which acted as a valve regulating the overpressure of deep magmatic fluids.

¹Istituto Nazionale di Geofisica Vulcanologia, Roma1, 00143 Rome, Italy. ²Istituto Nazionale di Geofisica Vulcanologia, ONT, 00143 Rome, Italy.

³Dipartimento di Scienze, Università degli studi Roma 3, Largo San Leonardo Murialdo Roma 1, 00146 Rome, Italy. ✉email: irene.bianchi@ingv.it

Determining the proximity of magma to the surface is a daunting challenge in volcanology. This is particularly important for densely inhabited volcano islands like Ischia, Italy (Fig. 1), where moderate-magnitude but shallow earthquakes, like the one of 21 August 2017, are tragic events, with alarming symptoms but also opportunities to better investigate magma dynamics. Source modeling and coseismic ruptures concur with the hypothesis of a complex rupture process with a primary non-double-couple component and a secondary normal faulting displacement locally emphasized by triggered landslides^{1–4}. The exceptional low-frequency content, low-stress drop (0.01 MPa), and low S/P spectral ratio suggest significant involvement of fluids³. The understanding of the connection between the earthquake and the shallow hydrothermal and deep magmatic systems is, therefore, crucial to reconstruct the state of the volcano.

The eruption history of the Ischia volcano is rather long, reconstructed only for its subaerial part from a span of 150 kyr^{5,6}. After an initial long period of mostly effusive activity, a series of Plinian to sub-Plinian eruptions and pyroclastic flows ensued, leading up to a main caldera-forming event at about 55 kyr⁷. The main ancient paroxysms were succeeded by cycles of activities dominated by specific differentiation processes of magmas accumulated within crustal reservoirs⁸. After the caldera collapse, an ultra-fast resurgence of the caldera floor resulted in an uplift of ~1000 m of the Mount Epomeo resurgent block⁹, whose pulsatory nature was evidenced by periods of increased gravitational instability and sector collapses^{10,11}.

The most recent volcanic cycle started at ca. 10 kyr after a prolonged quiescence (18–10 kyr), forming a monogenetic field made of latitic to alkali-trachytic lava domes and explosive centers mostly located along the densely populated eastern flank of the resurgent block¹². Until the last eruption which occurred in 1302 CE, the eruption frequency over the last 10 kyr has been one every 500 years, increasing to one every 100 years during the last 3 kyr¹². The largest eruption was the 122 CE sub-Plinian Cretaio eruption¹³. The uplift of the Mount Epomeo block since 50 ka, to a present-day elevation of 787 m a.s.l., is thought to have formed by an intrusion within a laccolitic magma chamber^{14,15} with a contribution of regional stress¹⁶.

The geothermal gradient at Ischia, which ranges between 150 and 220 °C/km, is driven by vigorous hydrothermal convection and is thought to indicate magmatic temperatures at 4–5 km depth¹⁷. The current ground deformation of the island shows a concentric pattern with a subsidence rate exceeding 10 mm/yr, measured by the Global Navigation Satellite System (GNSS), leveling, and multitemporal satellite interferometric data^{18–21}. Hydrothermal system depressurization with deep source deflating by degassing and magma cooling have been invoked as possible causes of the observed ground displacements in addition to a landslide of the unstable flanks.

Decades of monitoring helped define the gross features of the system but opened a tantalizing debate on the physical state and hazard of the volcano¹². We tend to ignore how the dynamics of the central sector relate to the volcano's current activity and its most recent eruptions. Do major moderate-magnitude but shallow and destructive earthquakes at the periphery of the resurgent block occur in response to magma dynamics? Is magma present and sizable beneath the volcano? All these questions need full addressing to estimate potential hazards bearing in mind that the current quiescence of the volcano is poorly understood²².

The largest and most devastating earthquake prior to the one of 2017 occurred in 1883 and caused the death of more than 2000 people²³. Apart from such rare disastrous events, the natural seismicity of the island is rather poor²⁴, lowering the efficacy of local earthquake tomography to investigate the volcano's plumbing system. The analysis of teleseismic data, therefore, becomes powerful in sounding the quiescent volcano and yielding a complete illumination of the crust^{25,26}.

Changing the classical concept of a magma chamber as a large volume of molten material to that of broad intra-crustal systems of connected magma bodies²⁷ implies that in order to capture where these molten materials are stocked, a few steps beyond the classical imaging of velocity perturbations should be considered. Domains molten into coalescing sets of low-aspect-ratio dikes can generate peculiar anisotropic signatures that stand up from seismically opaque volumes within which the average velocities are rather homogeneous. In this study, we use broadband data from two seismic stations on the island, IOCA and IMTC, operative

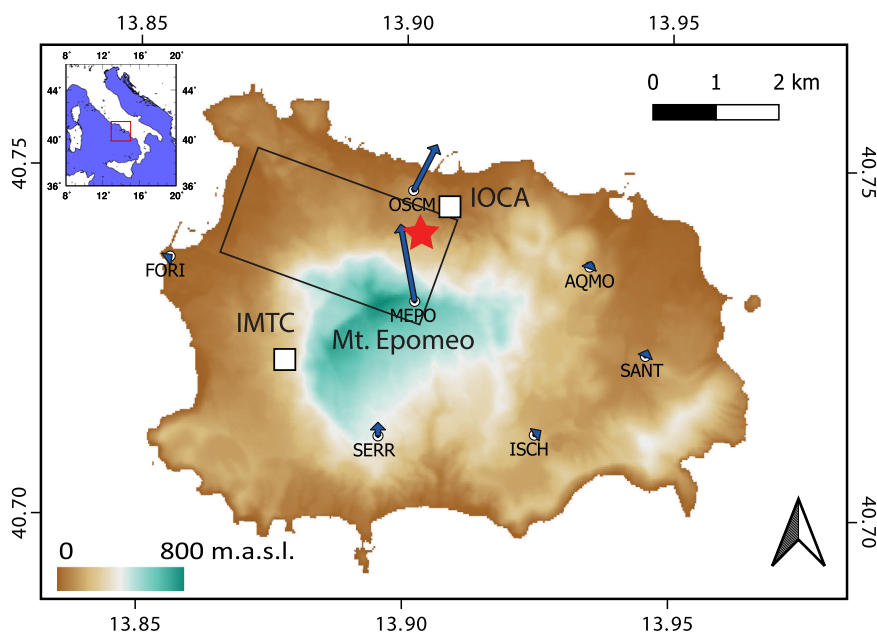


Fig. 1 Map of Ischia Island. Map of Ischia island showing the seismic stations' location (white squares). The white circles indicate the location of the GNSS stations at which the horizontal coseismic displacement is displayed by the blue arrows. The projection of the fault plane is shown as an empty rectangle. In the upper left corner the location of the island with respect to Italy.

since 2011 and 2015, respectively, to retrieve the S-wave velocity (V_s) and anisotropy structure with receiver functions (RFs) analyses in an attempt to better define Ischia's magmatic system.

Results

The $k = 0$ components of the RFs harmonics were used to retrieve a 1D shear-velocity model for each station with the help of a Reversible-jump Markov chain Monte Carlo (RjMCMC) scheme²⁸. The $k = 1$ components were scrutinized to infer the presence of anisotropy and dipping interfaces beneath each station using the Neighborhood Algorithm (NA)²⁹.

The $k = 0$ harmonics show the main isotropic pulses related to velocity discontinuities of the crust (Fig. 2). The P pulse is broadened at station IOCA in the first second, suggesting the presence of a shallow dipping plane and low V_s in the shallower layer(s). At station IMTC, the direct P pulse is clearly set at 0, while a second positive pulse in the first second indicates a shallow layer with high V_s . Clear positive pulses are present from the second to the fourth second at both stations. The first two seconds of the $k = 1$ components of the RFs harmonics are dominated by sharp pulses (Fig. 2), consistent with the presence of a shallow dipping layer and a deeper strong anisotropy, stronger at station IOCA.

While differing at lower depths, the 1D V_s models at stations IOCA and IMTC (Fig. 3) present similar features at depths larger than 5–6 km. This is consistent as rays at the two stations largely sample the same structure at depth and differ only in the shallower layers. IMTC shows a rapid increase of V_s from 2.5 km/s to about 3.5 km/s at a depth of 2 km. From here, the V_s remains mostly constant down to 10 km of depth, where it increases to >4.0 km/s and decreases only at $z = 20$ km. The Moho interface is reasonably in the depth range between 25 and 30 km. This layering shows similarities to the one at station IOCA but from 4 to 5 km downward. At shallower depths, the V_s is extremely low ($V_s < 2.0$ km/s), in agreement with the observed P pulse broadening.

The 3D model at station IOCA displays a dipping interface (strike N110°, dip 40°) at a depth of about 2.5 km and a 4 km thick anisotropic layer with fast symmetry axis oriented N290°, plunging 30°. The pulses due to the dipping interface and to the anisotropy within the $k = 1$ component of the RFs harmonics are shown in Supplementary Fig. S3. The signal on the cosine component is due to the dipping interface, while the anisotropy is responsible for the signal on the sine component. For the purpose of this study, the same anisotropy percentage for both primary (P) and shear (S) waves has been used for the modeling.

The lack of strong independent constraints and the prevalent not-double-couple component allow for the proliferation of very different and contradicting models for the 2017 earthquake source. The intriguing outcome of the RFs analysis spurred us to remodel the seismic source, constraining the fault geometry with an N110° striking SW-dipping plane. We performed a linear inversion of coseismic GNSS and Interferometric Synthetic Aperture Radar (InSAR) displacement data³ by using Okada's formalism³⁰ to retrieve the slip and closure distributions along the fault plane constrained by RFs data thus obtaining an excellent result in terms of data fit. Data fit comparison between RFs-constrained models and unconstrained ones are shown in the Supplementary Information file (Figs. S8–S12). Modeled GNSS displacements are in good agreement with observations both in the horizontal and vertical components (Fig. 4a and b). Synthetic SAR displacements (Fig. 4i–l) fit the observation satisfactorily with appreciable residuals only in a few zones affected by slope phenomena and in a limited area in the very near field (Fig. 4m–p). The latter misfit could be due to the planar simplification with respect to the strike

variation of the real faults in the field. Both volume variations and slip distribution (Fig. 4c and d, respectively) consist of super-imposable oblique patterns, which are complementary to each other along the shallow patches.

Discussion

Intensification of gas emission, seismicity, and ground deformation are symptoms continuously monitored to infer changes in the Ischia volcano dynamics^{19,31,32}. While the long-term deformation of the island consists of a central resurgence, and the high heat flow suggests magmatic temperatures at crustal levels, evidence for the presence of eruptible magma within the crust, like for most active volcanoes around the world, remains elusive. The decennial deflation of Mount Epomeo is also at odds with the long-term resurgence, suggesting that the island of Ischia is affected by cycles with different dynamics¹².

There is no doubt that the 2017 earthquake represents a relevant feature in the dynamics of the volcano. The shallow event has been modeled as a composite source with the involvement of fluids in the mechanism^{1,2}. The source modeling³ proposed a north-dipping normal fault lying above a closing sub-horizontal crack, while surficial sliding, induced by the seismic shaking, contributed to the observable ground deformation³³. Seismological data support the existence of a negative tensile crack with a minor double-couple component, consistent with a contraction at about 1 km b.s.l. This complex process is a response to the continuous decennial deflation of the volcano below the southern flank of Mount Epomeo²¹.

How such transient deformation episodes relate to the decennial deflation and magma dynamics is a major issue to unravel. Our results contribute to solving some puzzling features of the deep structure and the connection with the magmatic system. As expected, the V_s models of the two seismic stations are similar for depths >4–5 km as teleseismic rays sample the same deep structure of the volcano. Differences in the first pulses are evidence of local and strong lateral variability of the shallow structure.

From bottom to top, we observe the following:

- Deep low V_s in the lower crust ($V_s = 3.5$ km/s at 20 km),
- Exceptionally high V_s ($V_s = 4.2$ km/s at 7–13 km),
- Relatively high V_s zone at a depth between 3 and 7 km ($V_s = 3.5$ km/s), with a strong anisotropy of up to 14%,
- Shallow N110° striking, SW-dipping fault, well evident beneath station IOCA.

The deep low V_s is a common feature at the two stations and could be indicative of high temperatures in the lower crust since the V_s is much lower than average values at that depths³⁴. This heating could be related to the broad tectonic Quaternary extension of the Tyrrhenian margin and likely represents the deep root and the engine of the Ischia magma plumbing system.

The high V_s at 7–13 km depth is an intriguing feature that can be interpreted as a thick accumulation of mafic material by repeated magma underplating. This invites an intriguing scenario about how magma is added and stored within the crust during continental extension. Repeated episodes of magma ascent, emplacement, and solidification at mid-crustal depths might have occurred during the life of the volcano, progressively creating this massive accumulation²². The high-velocity body indicates that the intrusive complex is in sub-solidus conditions and may represent today a transfer zone for magmas formed in the deep roots of the plumbing system and traveling upward in the absence of wide melt volumes in the upper crust.

The upper central portion of the plumbing system at 3–7 km depth consists of a high V_s . It is a laterally heterogeneous complex of mostly solidified material, forming a broad system of hot

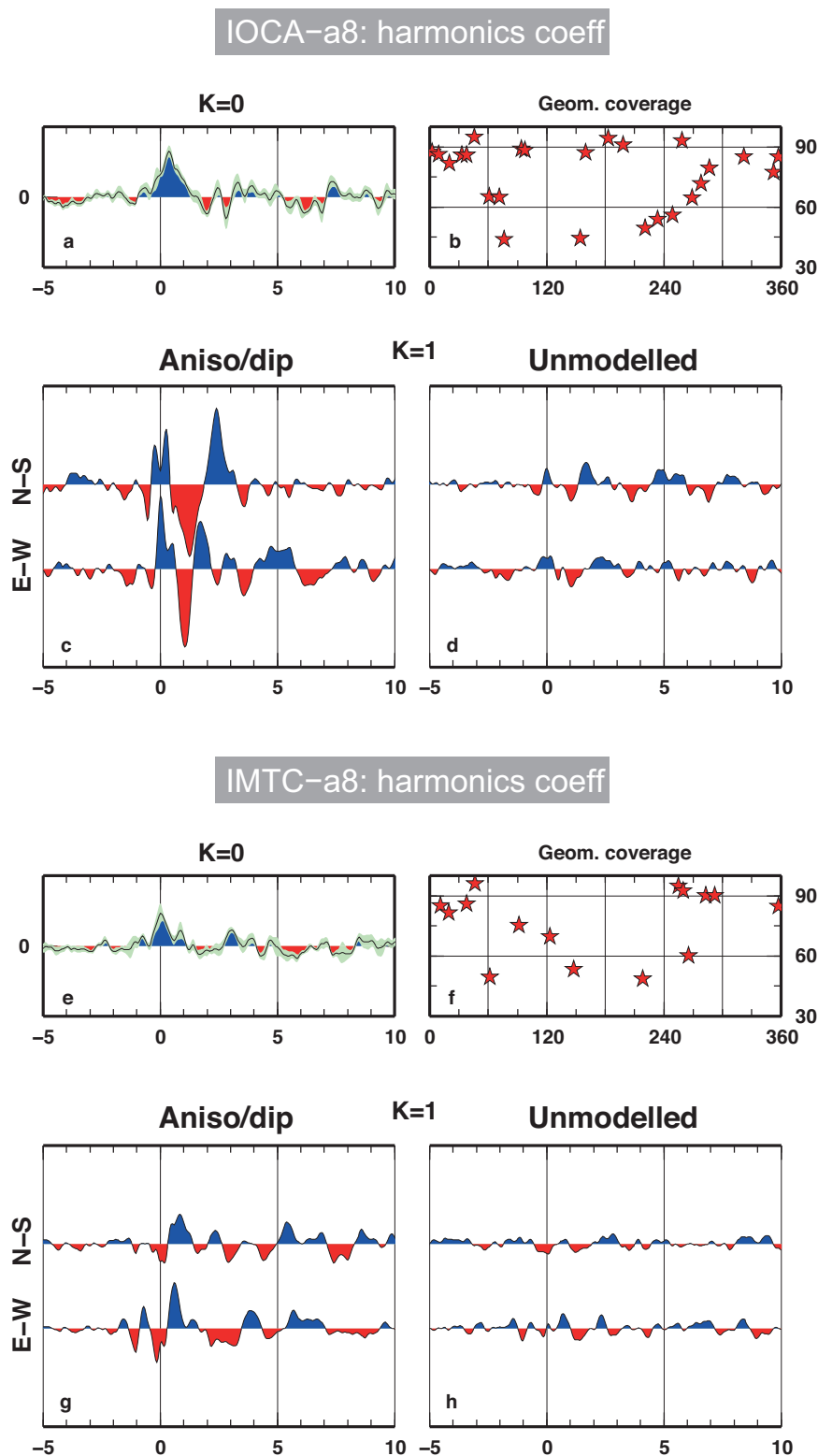


Fig. 2 Harmonic decomposition for the RFs data at the IOCA and IMTC stations. The $k = 0$ term is a weighted stack of the radial RFs (**a**, **e**), and epicentral distribution of the teleseisms used (**b**, **f**). The $k = 1$ term of the harmonic decomposition, as sum (**c**, **g**) and difference (**d**, **h**) of R and T. N-S and E-W labels indicate the cosine and sine terms of the harmonic decomposition, respectively.

crystal mushes^{35,36}. The strong anisotropy present here might indicate that the magma fills low aspect ratio dykes pervading the mush. The temporal coalescence of such dykes could favor peculiar episodes of pressurization that promote the instability of the system. The reconstructed scenario for the Ischia magma

plumbing system suggests the presence of a hot root zone at 20 km depth, a “brittle” transfer zone between 13 and 7 km, and a large viscoelastic crystal mush between 7 and 3 km, where magma is ephemerally present and variably interconnected²². The fabric of the anisotropy, defined by the plunge of the fast symmetry axis

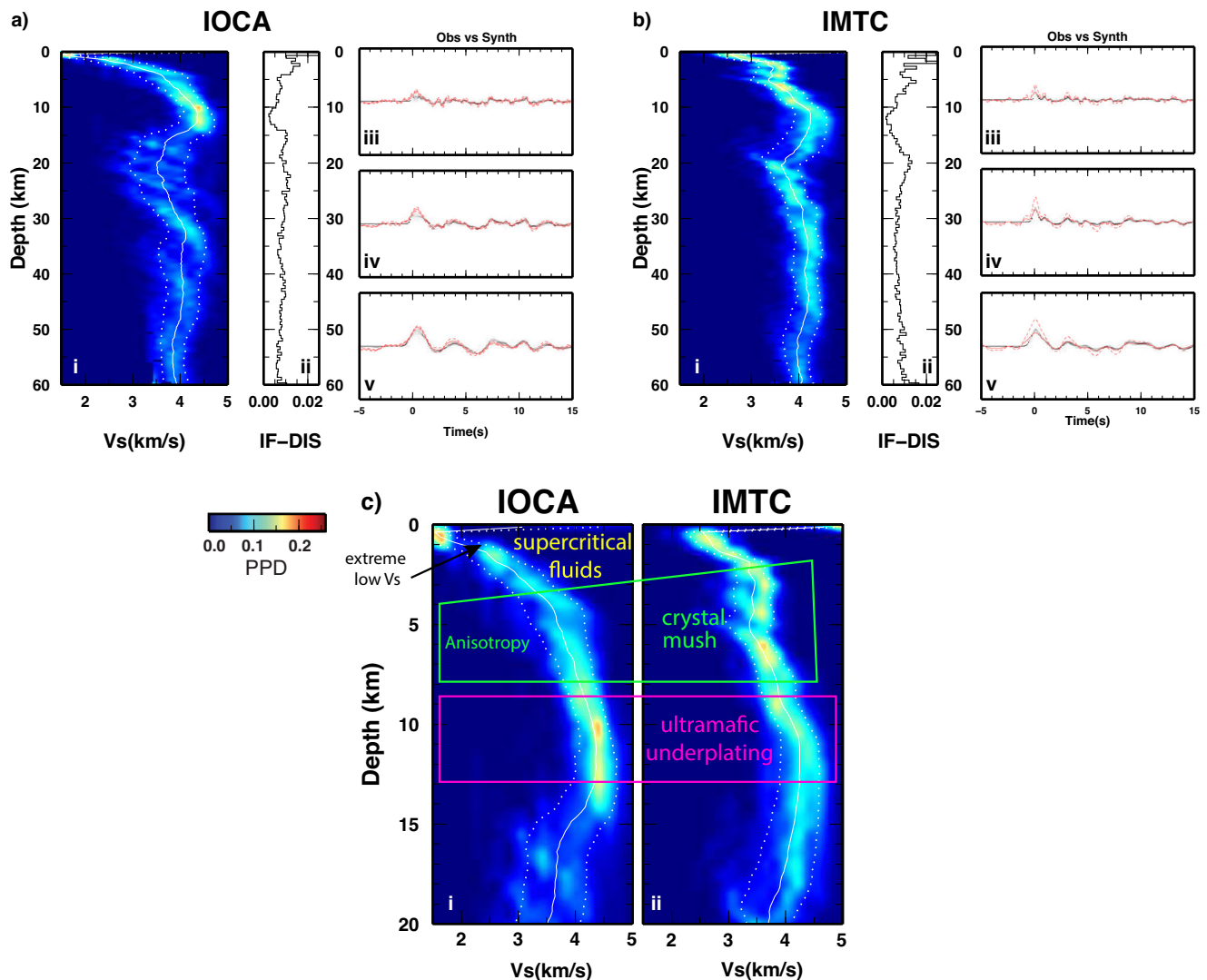


Fig. 3 Posterior probability density (PPD) profiles. PPD of the velocity with depth (panels i) for the stations IOCA (a) and IMTC (b), solid white line for the mean model, dashed lines mark the 95% confidence interval, and background color for the full PPD. Panels ii show the interface distribution at depth (IF-DIS). The fit between observed and synthetic RFs for the three Gaussian parameters (red for the observed and black for the synthetic RF) is shown in panels iii for Gaussian filter 8, iv for Gaussian filter 4, v for Gaussian filter 2. **c** Sketched interpretation of the velocities at depth for IOCA (c i) and IMTC (c ii).

N290°–30°, remarkably resembles the average strike and dip of the trapdoor post-caldera resurgence of the Ischia caldera floor with its hinge in the southern sector and highest displacement in the north^{16,37,38}. The anisotropic fabric reflects the plexus of inclined intrusions that progressively inflated the post-caldera crystal mush, driving the 1000 m caldera floor anisotropic resurgence. We, therefore, explain the evolution of the island as a result of repeated episodes of intrusions on such inclined planes, suggesting that this fabric also controls the present-day rise of magmatic fluids from below.

We modeled the 2017 earthquake on the shallow SW-dipping fault retrieved by the RFs, observing that a deep closure on the 110° striking plane with a shallow vertical normal slip well fits coseismic geodetic data and is consistent with seismological observations². We interpret this event as part of a process that involves the ascent of supercritical fluids from the shallow superhot volume channeled along the fault. Sharp seismic releases affected sudden negative tensile deformation along the fault, followed by a shallow vertical slip on the plane (Fig. 4). The extremely low Vs in the volume around the fault could further

explain the unusually long duration of the seismic source and the low-frequency content observed in seismograms³.

In our conceptual model (Fig. 5), the magmatic fluids raised within the hot crystal mush are controlled by the shallow fault. This is consistent with the different depth and fast axis azimuth (crack elongation) anisotropy found at IOCA. Episodic pulses of supercritical fluids in the superhot shallow volume with the sudden occurrence of moderate-magnitude, shallow, and complex earthquakes seem to have been the drivers behind the present-day deformation of the volcano. This process involved fluids released from melt-filled dykes present within the central crystal mush. While the fault acted as a pressure valve for the deep fluids, the crustal fabric controlled the recurrent inflation and deflation episodes.

Our study suggests that the detection of eruptible magma in active magmatic systems could elude our deeper understanding if we only consider classical seismic velocity imaging. An idealized, large, low-velocity chamber is not perceptible in the Ischia deep structure, as is the case of many other volcanoes. Nevertheless, a volume with strong anisotropy and relatively high velocity could

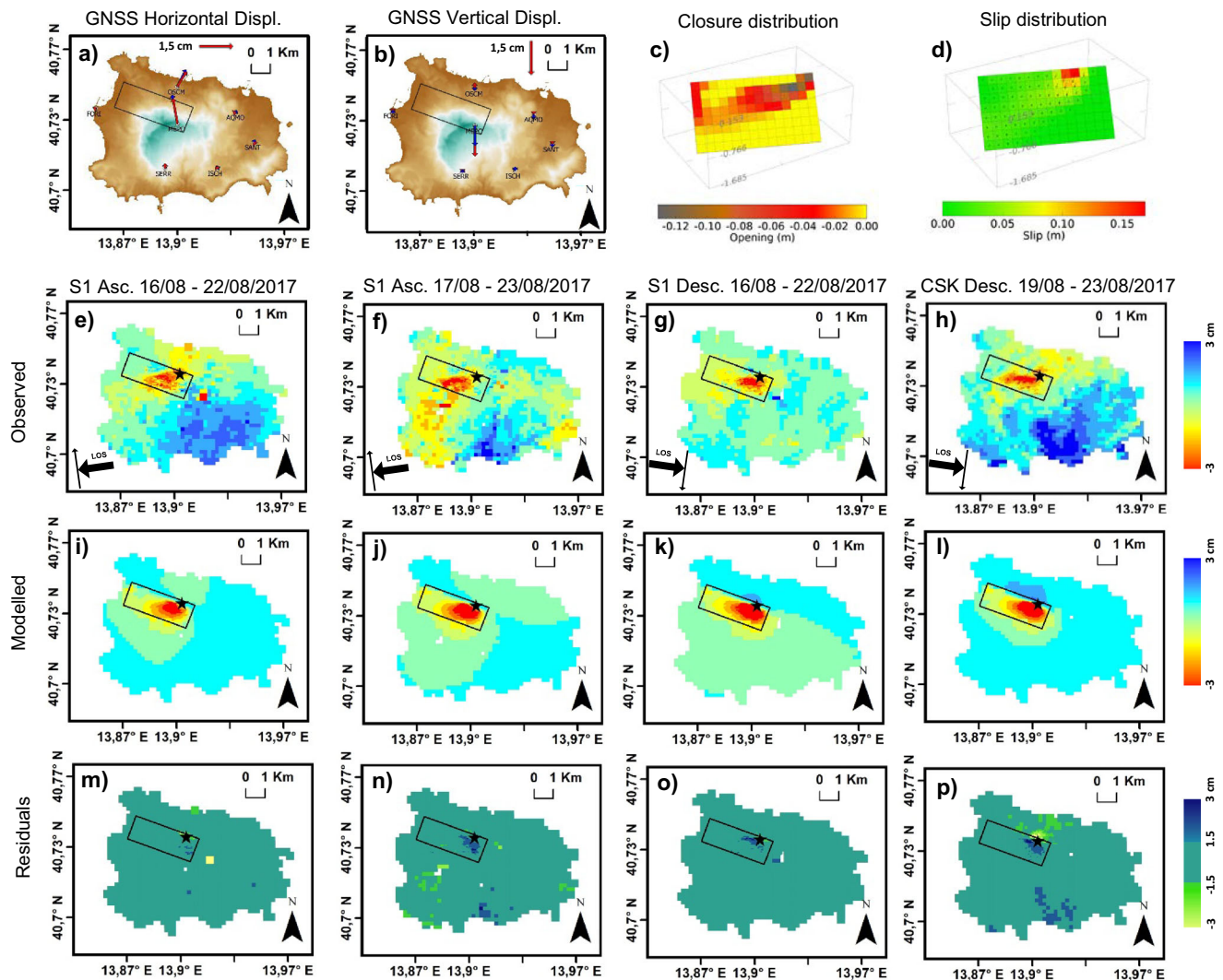


Fig. 4 Observed and modeled displacements of the 21 August 2017 earthquake. Horizontal (a) and vertical (b) GNSS coseismic displacements. The blue and red arrows represent, respectively, the observed and modeled vectors, at GNSS stations (white circles). The projection of the modeled fault plane is shown as an empty rectangle. c and d are, respectively, the 3D plots of modeled volume variations and slip distribution along the fault plane (on a 250×250 m grid), whose geometry is constrained by RFs results. Panels e–h present the LOS displacements relative to the ascending S1 (16–22 August 2017), ascending S1 (17–23 August 2017), descending S1 (16–22 August 2017), and descending CSK (19–23 August 2017); panels i–l report modeled LOS displacements whereas panels m–p show residual LOS displacements; satellite flight paths (black arrows) and LOS are represented; black rectangle is the projection of the modeled fault plane.

be indicative of magma residing in dykes within a diffuse, hot, but solidified, crystal mush that constitutes the principal feature of the crustal plumbing system (Fig. 5). This volume is the result of intrusions that progressively inflated the post-caldera crystal mush and whose progressive emplacement has been the driving force behind the 1000 m resurgence of the caldera floor. We suggest that both the longer and short-term evolution of the volcano are due to the emplacement of the same deep structures that have been regulating the volcanic resurgence in the last 55 kyr, and which control the present-day rise of magmatic fluids from below. Future monitoring of anisotropy variations could be used to infer the progression and migration of fluids and melts from the mush.

Data and methods

Receiver function (RFs) analysis. New local velocity models are built from passive seismic data recorded at two stations located

on the island of Ischia. In the absence of high frequencies from local volcanic sources, seismic records collected between 2016 and 2020, occurring at an epicentral distance between 30° and 100° with $M > 5.9$, were visually inspected and accepted or discarded depending on the S/N ratio. RFs were computed on traces downsampled to 20 sps and rotated to the RTZ reference system, where the radial (R) is computed along the great circle route between the epicenter and the station, positive away from the source, while the transverse (T) is positioned 90° clockwise from the R. The RFs are time series made of P-to-s converted phases^{39,40}, obtained by a deconvolution of the vertical component from the horizontal components of the seismogram. Here we applied the multiple Gaussian filters method⁴¹ (i.e., 2, 4, and 8, that limit the frequency band up to respectively about 1, 2, and 4 Hz) for the computation of the RFs dataset.

In Fig. 2, we show the back azimuthal harmonics of the RFs data^{42–44} as a function of the incoming P-wave direction³³. At every time step, an ensemble of RFs can be expressed as a scaled

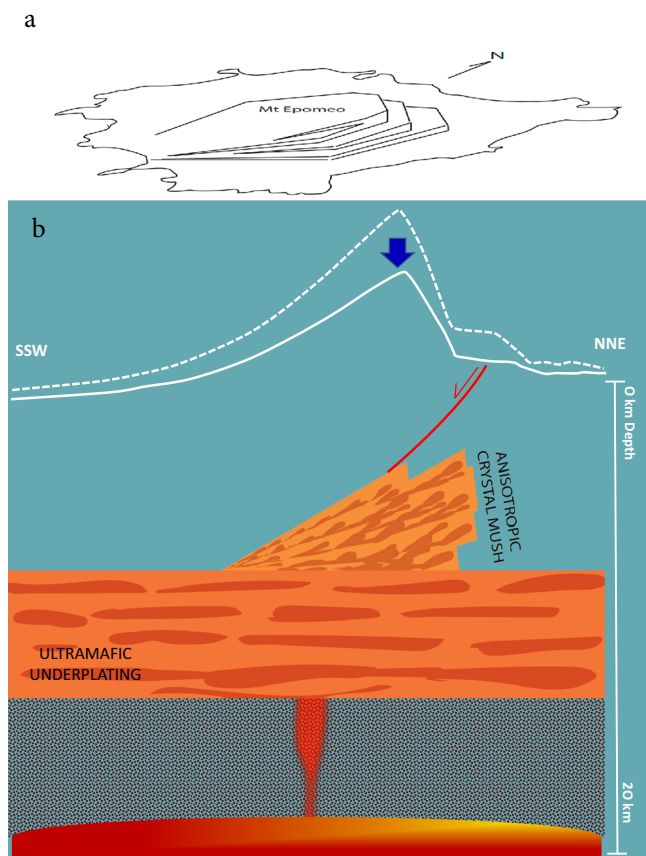


Fig. 5 SSW–NNE profile sketch of the structure below the volcano. 3D view and topographic height are drawn in panel **a** after Acocella and Funicello¹⁶. **b** The main 3D elements are schematically represented to visualize their respective location. From surface to bottom (down to 20 km) as follows: the N110° striking fault, the anisotropic crystal mush, and the mafic underplating.

sum of $\cos k\phi$ and $\sin k\phi$, where k is the harmonic degree (0 and 1 as shown here) and ϕ is the back azimuth. For each station, we obtained three gathers: the $k=0$ and the first order ($k=1$) harmonics (both in cosine and sine)^{45,46}. The cosine is here labeled N–S for easier interpretation given the fact that maximum amplitudes are occurring in this component when north or south-dipping interfaces or north–south trending anisotropy axes are present. The sine is labeled E–W as the maximum number of amplitudes that occur in this component whenever east or west dipping interfaces or east–west trending anisotropy axes are found.

Shear wave (S-wave) velocity models. To retrieve a 1D shear-velocity model for each station, we used the $k=0$ component of the RFs harmonics by applying a Reversible-jump Markov chain Monte Carlo (RjMcMC) scheme²⁹. In a second step, by employing the Neighborhood Algorithm (NA), we used the $k=1$ components to infer the presence of anisotropy and dipping interfaces beneath each station²⁸. The RjMcMC solved the non-linear inverse problem by the application of a trans-dimensional method exploring the misfit to the data within a large prior which defines the model space; the layer thicknesses and number of layers were freely explored by the algorithm.

We ran an RjMcMC search on 100 independent chains. For each chain, 200,000 random models were generated out of which 100,000 were discarded as part of the burn-in stage. As a result, we obtained 10^7 models to compute the posterior probability

density function (PPD) (Fig. 3). In this stage, we modeled the $k=0$ harmonics using a reflectivity code^{28,47}. We considered multiples from all layers to adequately constrain the overall S-wave profile using the $k=0$ harmonics.

Our mean posterior model is representative of the entire family of models visited by the RjMcMC. Subfamilies with specific characteristics are likely to be found in the ensemble of sampled models, and we show them in Figs. S4–S7 in the supplementary material.

From the PPD obtained for station IOCA (Fig. S1), we extracted a layered velocity model and used the fixed V_s values to infer the presence of dipping interfaces and anisotropy beneath the seismic station by means of the NA algorithm. We initially generated 100 samples from the parameter space. From the neighborhood of the 25 best-fit models, 50 new samples were iteratively resampled. After 50 iterations, we obtained an ensemble of 2600 models. Considering the presence of either (1) one inclined interface, (2) one anisotropic medium, or (3) both inclined interface and anisotropy, synthetic RFs for three samples were calculated using RAYSUM⁴⁸, including multiples, of the first layer only. The synthetics, computed with a Gaussian filter $a=8$ and compared to the observed RFs are displayed in Fig. S3. In this second step, we did not consider multiples from deeper layers since multiples from anisotropic layers are likely to be disrupted by the lateral heterogeneity of the layers' physical properties, even more than in isotropic ones. In other words, the stable and constant orientation of the anisotropic materials in rather large portions of the crust is unlikely and this does not allow retrieving coherent multiples from all baz directions.

Non-uniqueness of the S-wave velocity models. The RFs inversion problem is known to be inherently non-unique. Linearized inversion approaches have been applied for decades, but they fail to address the critical aspect of the problem. Monte Carlo approaches, like the one adopted here, have been introduced to tackle exactly this drawback of previous inversion schemes.

Monte Carlo approaches are applied to obtain repeated solutions of the forward problem for a number of different combinations of the investigated parameters. The final result is a family of sampled models, drawn from the posterior probability distribution, which equally fits the observed data ($k=0$ harmonics in this case). From this family, one can extract a number of relevant estimators, like the mean-posterior model (red line in Figs. S4–S7, and white solid lines in Fig. 3), or the 1D marginal V_s distribution at depth (grayscale in Figs. S4–S7 and color scale in Fig. 3).

Other relevant information about the plumbing system of the Ischia Island volcano can also be retrieved. For instance, we have the possibility to test how the velocity at around Moho depth (~20 km) is constrained by the RF data and how it influences the V_s profile. To fulfill this task, we separated the family of sampled models into two sub-families: (1) subfamily A consisting of models with average V_s lower than 3.5 km/s at depths between 18 and 22 km, and (2) a complementary subfamily B of models where the average V_s are higher than 3.5 km/s at depths between 18 and 22 km (Figs. S6 and S7).

Our analysis clearly shows that both high and low velocity at Moho depth is consistent with the data (54% and 46% of the two subfamilies in the case of IOCA, respectively), with V_s decreasing in both cases at depths between 15 and 25 km. Moreover, the V_s at the Moho trades off with the minimum V_s value, in fact, the low-velocity layer is shallower for subfamily A.

We could further test the hypothesis that V_s is lower in the accumulation of mafic material around depths of 10 km by separating the models of the family with an average V_s lower than

3.9 km/s between 7- and 13 km depth from the other sampled models (Figs. S4 and S5, panel c). In so doing, we could observe if the relevant features discussed above were still present in the subfamily, or if such a subfamily displayed different features, changing the physical properties of the mean posterior model. In Figs. S4 and S5, we show that the two families with different Vs in the accumulated mafic material (depth range 7–13 km) are very similar. However, the number of models in the family with a velocity lower than 3.9 km/s is very limited (0.8%), which indicates that such a feature, i.e., high velocity in the mafic accumulated material, is strongly constrained by the data.

Geodetic modeling of the 2017 source. The intriguing outcome of the RFs analysis spurred us to remodel the seismic source responsible for the 2017 Ischia earthquake, constraining the fault with an N110° striking SW-dipping plane constrained by RFs. We jointly inverted the GNSS (Fig. 4a and b) and InSAR coseismic displacements by using an elastic, isotropic, and homogeneous model. In our case, the interferometric SAR dataset constitutes of pairs from Sentinel-1 (S1) satellites processed by using single-pair differential SAR interferometry approach⁴⁹: two C-band S1 pairs in ascending geometry from 16–22 and 17–23 August 2017 (Fig. 4e and f, respectively Supplementary Data 1 and 2), and one pair in descending geometry from 16 to 22 August 2017 (Fig. 4g Supplementary Data 3). We also included a descending X-band COSMO-SkyMed (CSK) pair spanning 17–23 August 2017 (Fig. 4h, Supplementary Data 4). The GNSS data are in Cartesian reference and the SAR measurements are in satellites line of sight (LOS) relative to the ascending and descending orbits. To avoid loss of SAR data coverage and approximation due to the north component assumption, we directly modeled the LOS displacement. The original InSAR unwrapped interferograms were subsampled on a space grid of 200 × 200 m and reduced to 50 × 50 m in the near field to obtain about 3000 points for each dataset. To prevent the effect of coseismic landslides, we associated an increasing uncertainty proportional to the landslide probability^{3,33}.

Since previous models and seismological observations suggest a complex source³, we applied a two-step approach consisting of a non-linear inversion for the best-fit source parameters, followed by a linear inversion for slip and closure distribution along the fault plane. The source geometry was constrained by the RFs results, with the non-linear step providing for the rake angle and the geometry refinements.

Data availability

Telesismic waveforms are available on the EIDA website (<https://doi.org/10.13127/SD/X0FXNH7QFY>)⁵⁰. Sentinel1 satellite Single Look Complex (SLC) images are copyright of the European Space Agency and available on the Copernicus website (<https://dataspace.copernicus.eu/>). COSMO-SkyMed satellite Single Look Complex (SLC) images are copyrighted by the Italian Space Agency (ASI). Coseismic Sentinel 1 and COSMO-SkyMed displacements are from Calderoni et al. (2018) (<https://doi.org/10.1029/2018JB016431>) and are also reported as Supplementary Table S1 and as a Data set. Coseismic GNSS solutions from Calderoni et al. (2018) (<https://doi.org/10.1029/2018JB016431>) are reported in Figure S8; Raw GNSS data are available on INGV RING network website (<http://ring.gm.ingv.it; ftp://bancadati2.gm.ingv.it:2121/OUTGOING/RINEX30/RING/>).

Received: 2 August 2022; Accepted: 19 July 2023;
Published online: 29 August 2023

References

- De Novellis, V. et al. The 21 August 2017 Ischia (Italy) earthquake source model inferred from seismological, GPS, and DInSAR measurements. *Geophys. Res. Lett.* **45**, 2193–2202 (2018).
- Braun, T., Famiani, D. & Cesca, S. Seismological constraints on the source mechanism of the damaging seismic event of 21 August 2017 on Ischia Island (Southern Italy). *Seismol. Res. Lett.* **89**, 1741–1749 (2018).
- Calderoni, G. et al. Seismic and geodetic evidences of a hydrothermal source in the Md 4.0, 2017, Ischia earthquake (Italy). *J. Geophys. Res.: Solid Earth* **124**, 5014–5029 (2019).
- Nazeri, S., Zollo, A., Adinolfi, G. M., Amoroso, O., & Picozzi, M. The 2017 Ischia Earthquake (Southern Italy): source mechanism and rupture model from the inversion of a near-source strong motion record. *IEEE Trans. Geosci. Remote Sens.* **60**, 1–10 (2021).
- de Vita, S., Sansivero, F., Orsi, G., Marotta, E., & Piochi, M. Volcanological and structural evolution of the Ischia resurgent caldera (Italy) over the past 10 k.y. In *Stratigraphy and Geology of Volcanic Areas* Chap. 10, 464 (ed T. G. S. O. A. S. Papers) (Geological Society of America, United States, 2010).
- Sbrana, A., Marianelli, P. & Pasquini, G. Volcanology of Ischia (Italy). *J. Maps* **14**, 494–503 (2018).
- Brown, R. J., Orsi, G. & de Vita, S. New insights into Late Pleistocene explosive volcanic activity and caldera formation on Ischia (southern Italy). *Bull. Volcanol.* **70**, 583–603 (2008).
- Civetta, L., Gallo, G. & Orsi, G. Sr- and Nd-isotope and trace-element constraints on the chemical evolution of the magmatic system of Ischia (Italy) in the last 55 ka. *J. Volcanol. Geotherm. Res.* **46**, 213–230 (1991).
- Orsi, G., Gallo, G. & Zanchi, A. Simple-shearing block resurgence in caldera depression. A model from Pantelleria and Ischia. *J. Volcanol. Geotherm. Res.* **47**, 1–11 (1991).
- Tibaldi, A. & Vezzoli, L. The space problem of caldera resurgence: an example from Ischia Island, Italy. *Geol. Rundsch.* **87**, 53–66 (1998).
- de Vita, S., Sansivero, F., Orsi, G. & Marotta, E. Cyclical slope instability and volcanism related to volcano-tectonism in resurgent calderas: the Ischia Island (Italy) case study. *Eng. Geol.* **86**, 148–165 (2006).
- Selva, J. et al. Multiple natural hazards at volcanic islands: a review for the Ischia volcano (Italy). *J. Appl. Volcanol.* **8.1**, 1–43 (2019).
- Primerano, P., Giordano, G., Costa, A., de Vita, S. & Di Vito, M. A. Reconstructing fallout features and dispersal of Cretaio Tephra (Ischia Island, Italy) through field data analysis and numerical modelling: implications for hazard assessment. *J. Volcanol. Geotherm. Res.* **415**, <https://doi.org/10.1016/j.jvolgeores.2021.107248> (2021).
- Carlino, S., Cubellis, E., Luongo, G. & Obrizzo, F. On the mechanics of caldera resurgence of Ischia island (southern Italy). In *Mechanism of Activity and Unrest at Large Calderas* (eds Troise, C., De Natale, G. & Kilburn, C.R.J.) *Geological Society Special Publication* Vol. 269, 181–193 (2006).
- Galetto, F., Acocella, V. & Caricchi, L. Caldera resurgence driven by magma viscosity contrasts. *Nat. Commun.* **8**, 1–11 (2017).
- Acocella, V. & Funicello, R. The interaction between regional and local tectonics during resurgent doming: the case of the island of Ischia, Italy. *J. Volcanol. Geotherm. Res.* **88**, 109–123 (1999).
- Carlino, S. et al. The geothermal system of Ischia Island (southern Italy): Critical review and sustainability analysis of geothermal resource for electricity generation. *Renew. Energy* **62**, 177–196 (2014).
- Manzo, M. et al. Surface deformation analysis in the Ischia Island (Italy) based on spaceborne radar interferometry. *J. Volcanol. Geotherm. Res.* **151**, 399–416 (2006).
- Trasatti, E. et al. Magma degassing as a source of long-term seismicity at volcanoes: the Ischia island (Italy) case. *Geophys. Res. Lett.* **46**, 4421–4429 (2019).
- Beccaro, L. et al. Multitemporal and multisensor InSAR analysis for ground displacement field assessment at Ischia Volcanic Island (Italy). *Remote Sens.* **13**, 4253 (2021).
- Galvani, A., Pezzo, G., Sepe, V. & Ventura, G. Shrinking of Ischia Island (Italy) from long-term geodetic data: implications for the deflation mechanisms of resurgent calderas and their relationships with seismicity. *Remote Sens.* **13**, 4648 (2021).
- Giordano, G. & Caricchi, L. Determining the state of activity of transcrustal magmatic systems and their volcanoes. *Annu. Rev. Earth Planet. Sci.* **50**, 231–259 (2022).
- Carlino, S., Cubellis, E. & Marturano, A. The catastrophic 1883 earthquake at the island of Ischia (southern Italy): macroseismic data and the role of geological conditions. *Nat. Hazards* **52**, 231 (2010).
- D’Auria, L. et al. The seismicity of Ischia Island. *Seismol. Res. Lett.* **89**, 1750–1760 (2018).
- Piana Agostinetti, N. & Chiarabba, C. Seismic structure beneath Mt Vesuvius from receiver function analysis and local earthquakes tomography: evidences for location and geometry of the magma chamber. *Geophys. J. Int.* **175**, 1298–1308 (2008).
- Bianchi, I., Piana Agostinetti, N., De Gori, P. & Chiarabba, C. Deep structure of the Colli Albani Volcanic District (central Italy) from receiver function analysis. *J. Geophys. Res.* **113**, B09313 (2008).

27. Cashman, K. V., Sparks, R. S. J. & Blundy, J. D. Vertically extensive and unstable magmatic systems: a unified view of igneous processes. *Science* **355**, eaag3055 (2017).
28. Sambridge, M. Geophysical inversion with a neighbourhood algorithm—I. Searching a parameter space. *Geophys. J. Int.* **138**, 479–494 (1999).
29. Piana Agostinetti, N. & Malinverno, A. Assessing uncertainties in high-resolution, multifrequency receiver-function inversion: a comparison with borehole data. *Geophysics* **83**, KS11–KS22 (2018).
30. Okada, Y. Surface deformation due to shear and tensile faults in a half-space. *Bull. Seismol. Soc. Am.* **75**, 1135–1154 (1985).
31. Di Napoli, R. et al. A model for Ischia hydrothermal system: evidences from the chemistry of thermal groundwaters. *J. Volcanol. Geotherm. Res.* **186**, 133–159 (2009).
32. Chiodini, G. et al. Fumarolic and diffuse soil degassing west of Mount Epomeo, Ischia, Italy. *J. Volcanol. Geotherm. Res.* **133**, 291–309 (2004).
33. Albano, M. et al. The relationship between InSAR coseismic deformation and earthquake-induced landslides associated with the 2017 Mw 3.9 Ischia (Italy) earthquake. *Geosciences* **8**, 303 (2018).
34. Christensen, N. I. & Mooney, W. D. Seismic velocity structure and the composition of the continental crust: a global view. *J. Geophys. Res.* **100**, 9761–9788 (1995).
35. Cashman, K. V. & Giordano, G. Calderas and magma reservoirs. *J. Volcanol. Geotherm. Res.* **288**, 28–45 (2014).
36. Cooper, K. M. What does a magma reservoir look like? The ‘crystal’s-eye’ view. *Elements* **13**, 23–28 (2017).
37. Orsi, G., de Vita, S. & Di Vito, M. The restless, resurgent Campi Flegrei nested caldera (Italy): constraints on its evolution and configuration. *J. Volcanol. Geotherm. Res.* **74**, 179–214 (1996).
38. Carlino, S. et al. The volcano-tectonics of the northern sector of Ischia Island Caldera (Southern Italy): resurgence, subsidence and earthquakes. *Front. Earth Sci.* <https://doi.org/10.3389/feart.2022.730023> (2022).
39. Langston, C. A. Structure under Mount Rainier, Washington, inferred from teleseismic body waves. *J. Geophys. Res.* **84**, 4749–4762 (1979).
40. Ammon, C. J., Randall, G. E. & Zandt, G. On the non-uniqueness of receiver function inversions. *J. Geophys. Res.* **95**, 15303–15318 (1990).
41. Di Bona, M. Variance estimate in frequency-domain deconvolution for teleseismic receiver function computation. *Geophys. J. Int.* **134**, 634–646 (1998).
42. Park, J. & Levin, V. Anisotropic shear zones revealed by back azimuthal harmonics of teleseismic receiver functions. *Geophys. J. Int.* **207**, 1216–1243 (2016).
43. Girardin, N. & Farra, V. Azimuthal anisotropy in the upper mantle from observation of P-to-S converted phases: application to southeast Australia. *Geophys. J. Int.* **133**, 615–629 (1998).
44. Farra, V. & Vinnik, L. Upper mantle stratification by P and S receiver functions. *Geophys. J. Int.* **141**, 699–712 (2000).
45. Bianchi, I., Park, J., Piana Agostinetti, N. & Levin, V. Mapping seismic anisotropy using harmonic decomposition of receiver functions: an application to Northern Apennines, Italy. *J. Geophys. Res.* **115**, B12317 (2010).
46. Bianchi, I., Bokelmann, G. & Shiomi, K. Crustal anisotropy across northern Japan from receiver functions. *J. Geophys. Res. Solid Earth* **120**, 4998–5012 (2015).
47. Shibutani, T., Sambridge, M. & Kennett, B. Genetic algorithm inversion for receiver functions with application to crust and uppermost mantle structure beneath eastern Australia. *Geophys. Res. Lett.* **23**, 1829–1832 (1996).
48. Frederiksen, A. W. & Bostock, M. G. Modeling teleseismic waves in dipping anisotropic structures. *Geophys. J. Int.* **141**, 401–412 (2000).
49. Massonnet, D. & Feigl, K. L. Radar interferometry and its application to changes in the Earth’s surface. *Rev. Geophys.* **36**, 441–500 (1998).
50. Istituto Nazionale di Geofisica e Vulcanologia (INGV). *Rete Sismica Nazionale (RSN)* <https://doi.org/10.13127/SD/X0FXNH7QFY> (Istituto Nazionale di Geofisica e Vulcanologia (INGV), 2005).

Acknowledgements

The authors wish to thank M. Apostolova for her assistance and advice in editing this paper. This research was funded in part, by the Austrian Science Fund (FWF) J4314-N29. For the purpose of open access, the author has applied a CC BY public copyright licence to any Author Accepted Manuscript version arising from this submission.

Author contributions

The authors confirm their contribution to the paper as follows: model computation, figure production, and text editing: I.B.; Geodetic inversion and text editing: G.P.; Experimental design, concept elaboration, and text editing: C.C.; Concept elaboration and text editing: G.G.

Competing interests

The authors declare no competing interests.

Additional information

Supplementary information The online version contains supplementary material available at <https://doi.org/10.1038/s43247-023-00938-8>.

Correspondence and requests for materials should be addressed to Irene Bianchi.

Peer review information *Communications Earth & Environment* thanks the anonymous reviewer(s) for their contribution to the peer review of this work. Primary Handling Editor: Joe Aslin.

Reprints and permission information is available at <http://www.nature.com/reprints>

Publisher’s note Springer Nature remains neutral with regard to jurisdictional claims in published maps and institutional affiliations.



Open Access This article is licensed under a Creative Commons Attribution 4.0 International License, which permits use, sharing, adaptation, distribution and reproduction in any medium or format, as long as you give appropriate credit to the original author(s) and the source, provide a link to the Creative Commons licence, and indicate if changes were made. The images or other third party material in this article are included in the article’s Creative Commons licence, unless indicated otherwise in a credit line to the material. If material is not included in the article’s Creative Commons licence and your intended use is not permitted by statutory regulation or exceeds the permitted use, you will need to obtain permission directly from the copyright holder. To view a copy of this licence, visit <http://creativecommons.org/licenses/by/4.0/>.

© The Author(s) 2023